Experimental Investigation on Hybrid Rocket Engines Using Highly Aluminized Fuels

Hendrik R. Lips*
DFVLR Institute for Chemical Propulsion and Engineering, Hardthausen, West Germany

The development of a hybrid rocket motor based on highly aluminized fuels and FLOX oxidizers is described. By using fluorinated oxidizers, volatile aluminum fluorides are formed as the main combustion product, which results in a higher combustion efficiency of the aluminized fuels than with oxygen-based oxidizers. Critical motor components such as oxidizer injector, mixing diaphragm, reaction chamber, and nozzle were developed to withstand the high temperature and the extremely corrosive combustion products. Correlations between the fuel regression rate and oxidizer mass flux are obtained. The interrelationship between aluminum loading and oxidizer composition and motor configuration on combustion efficiency is given.

Nomenclature

a	= regression rate coefficient
A_e/A_t	= nozzle area ratio
A_p	= fuel grain port area
c^*_{exp}	= delivered characteristic velocity
c^*_{th}	= theoretical characteristic velocity
CTPB	= carboxy-terminated polybutadiene
F	= measured thrust
FLOX-90	= 90 wt% fluorine/10 wt% oxygen liquid mixture
$\dot{G}_{ox}$	= oxidizer mass flux
$\dot{G}_t$	= propellant mass flux
Is_{th}	= theoretical specific impulse
Is_{exp}	= delivered specific impulse
I_{tot}	= delivered total impulse
L_F	= grain length
L^*	= reaction chamber characteristic length
$\dot{m}_F$	= fuel mass flow rate
$\dot{m}_o$	= oxidizer mass flow rate
Δm_F	= fuel weight loss
Δm_o	= consumed oxidizer
Δm_p	= consumed propellant
n	= regression rate exponent
O/F	= oxidizer/fuel mixture ratio
p_c	= chamber pressure
PU	= polyurethane
$\dot{r}$	= fuel regression rate
$\bar{\dot{r}}_e$	= average regression rate of aft one-third of the grain
$\bar{\dot{r}}_{\Delta m}$	= average regression rate over entire length
$\bar{\dot{r}}_{\Delta R}$	= grain port diameter average regression rate
R_0	= initial grain-port radius
ΔR	= consumed web
t_b	= burning time
t_v	= oxidizer valve action time
x	= location for grain-port diameter measurement
ρ	= fuel grain density
η_{c^*}	= combustion efficiency = c^*_{exp}/c^*_{th}
η_{Is}	= specific impulse efficiency = Is_{exp}/Is_{th}

Presented as Paper 76-640 at the AIAA/SAE 12th Propulsion Conference, Palo Alto, Calif., July 26-29, 1976; submitted Aug. 30, 1976; revision received April 15, 1977.

Index categories: Solid and Hybrid Rocket Engines; Structural Materials; Combustion and Combustor Designs.

*Research and Development Engineer, Missile Propulsion Section, German Aerospace Research Establishment.

Introduction

THE performance of hybrid-propellant rocket motors can be improved by adding aluminum to the solid fuel. Theoretical calculations show that the specific impulse increases with increasing aluminum loading. However, performance evaluation of preliminary motor firings using highly aluminized solid fuels and liquid oxygen indicated that very poor combustion efficiencies were obtained; the delivered characteristic velocity decreased with increasing aluminum loading.

High-speed photographs and chemical analyses of exhaust product samples indicated that the aluminum particles were discharged from the nozzle with only partial combustion. The incomplete aluminum combustion is largely due to inhibition of the heterogeneous surface oxidation of the metal particles by the formation of a protective high-melting-point aluminum oxide coating, which serves as an effective barrier to mass diffusion and energy transfer to the burning particle.

To provide more information for selection of an optimal propellant combination, transparent slab burner tests were performed in order to identify the role of the propellant composition on the combustion behavior, including the effects of 1) oxidizer composition, 2) polymer binder type, 3) metal type, and 4) metal loading. The results of these tests are described in Ref. 1.

One of the principal conclusions of the investigation described herein is that aluminized fuels combusted with highly fluorinated oxidizers yield volatile aluminum fluorides as the main combustion product. This results in more efficient combustion of the aluminum particles, because there is no problem with retardation of the reaction by accumulation of condensed reaction products on the particle surface, as is the case with oxygen-based oxidizers.

Based upon the results obtained in Ref. 1, two high-energetic, hybrid-propellant combinations, consisting of highly aluminized solid fuels and liquid fluorine/oxygen mixtures (called FLOX) as oxidizer, were selected for subsequent motor firings. These compositions are 1) 60 wt% Al/40 wt% PU as solid fuel with FLOX-40 as oxidizer, which yields gaseous AlOF (aluminum oxyfluoride) as the main combustion product; and 2) 80 wt% Al/20 wt% PU as solid fuel with FLOX-90 as oxidizer, which results in gaseous AlF_3 (aluminum trifluoride) as the main combustion product.

The investigations presented in this paper were conducted in order to verify the predicted combustion efficiency increase and to determine a correlation between the oxidizer mass flux and the fuel regression rate.

Experimental rocket engines of 150 and 400 N thrust were used for the static test firings. The rocket engines were cooled

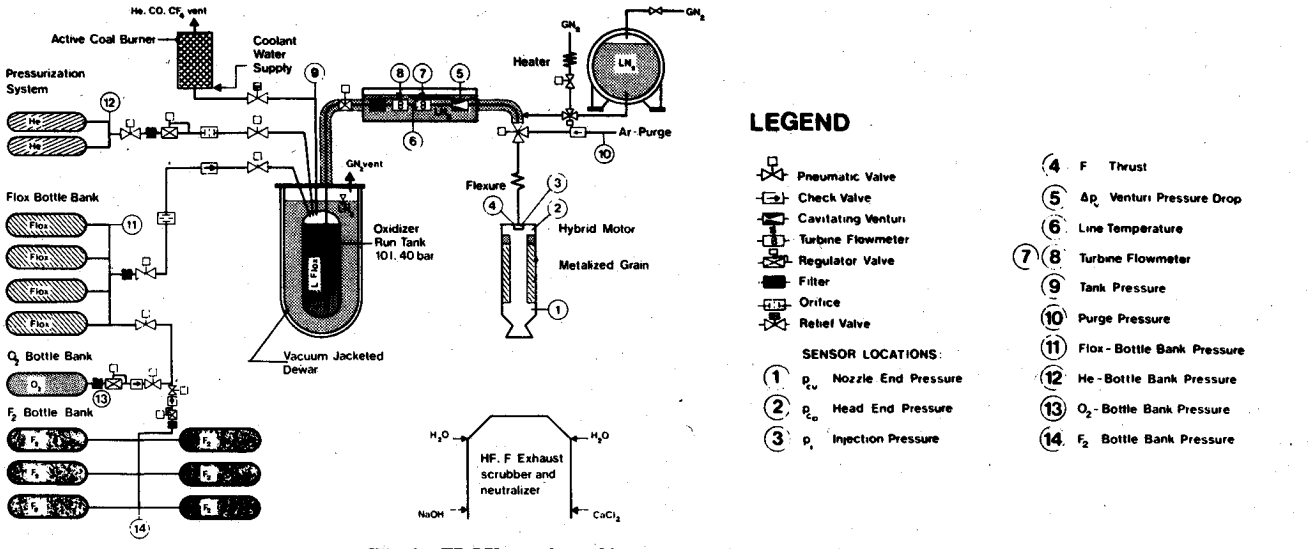

Fig. 1 FLOX supply and instrumentation schematic.

ablatively to keep the wall temperature of the chamber and nozzle high enough to prevent condensation of aluminum deposits. Critical motor components such as oxidizer injector, mixing diaphragm, reaction chamber, and nozzle throat insert, which could withstand the extremely corrosive combustion products, were developed and tested in a series of preliminary tests.

Test Facility and Preparation

All test firings were conducted using a vertical test stand. A schematic diagram of the flow system arrangement is shown in Fig. 1. Fluorine and oxygen gas are taken from a battery of commercially available bottles and are reduced and mixed in the FLOX bank. The gas mixture is liquified in the liquid-nitrogen (LN_2)-cooled run tank, and the oxidizer tank is pressurized by helium. The oxidizer feed line has an LN_2 jacket to keep the liquid FLOX below the boiling temperature. Argon is used to purge the oxidizer line and the injector, to quench the flame immediately after each run, and to chill the ablatively cooled motor components in order to reduce the soak-back time. All components of the FLOX-line system have to be passivated using low-pressure fluorine gas prior to each test.

Experimental Engine

The ablatively cooled motors consist of a solid fuel grain case of 35-cm length, an aft closure assembly containing the mixing diaphragm, reaction chamber, and nozzle, and a front closure assembly with an injector and splash-block as presented in Fig. 2. This simple design permits easy installation and exchange of the solid fuel, the injector, and the nozzle.

Hybrid Fuel Processing

The fuel grains are prepared using either carboxyl-terminated polybutadiene (CTPB) or hydroxyl-terminated polyester-polyurethane (PU) as polymer binder. These 60- to 80-wt% aluminized polymer binders are mixed, cast, vibrated, de-aerated under vacuum, and cured in the same manner as conventional composite solid-propellant grains. The pourable fuel usually was cast in a phenolic-impregnated paper tube, and, after polymerization, the fuel grain cartridge was loaded into the hybrid test motor.

Injector

Several test firings were made to optimize the spray pattern of the injector system. The best uniformity of the axial regression profiles of the solid grain was achieved using a vortex-barrier film injector, as shown in Fig. 3. To reduce injector head-end impingement effects further, a splash-block was added. In order to assess the impingement effect of the vortex momentum on the splash-block regression rate, the vortex-barrier ring diameter was varied, and a very slowly regressing, highly erosion resistant, aluminized polyimid solid fuel was used. To assure equal regression rates of the splash-block and the fuel grain, the regression rate of the splash-block was optimized by varying the aluminum loading.

Slightly higher overall average fuel regression rates were obtained due to partial pre-evaporation of the liquid FLOX film in the splash-block section before it entered the fuel grain. The subsequent optimization tests resulted in a more uniform fuel regression both axially and radially, as is illustrated vividly in Fig. 4.

Mixing Diaphragm

The gas flow pattern produced in hybrid combustion is stratified into an oxidizer-rich core region, containing unreacted fluorine and oxygen species, and a peripheral fuel-

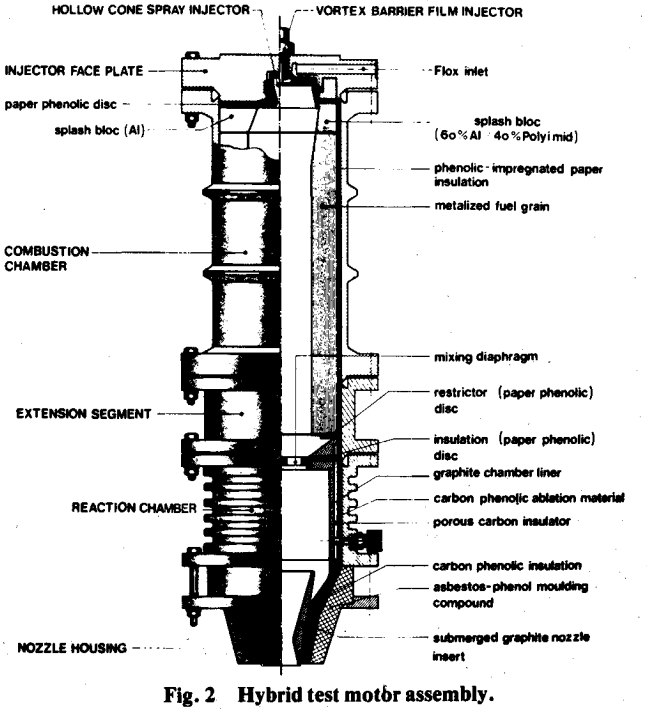

Fig. 2 Hybrid test motor assembly.

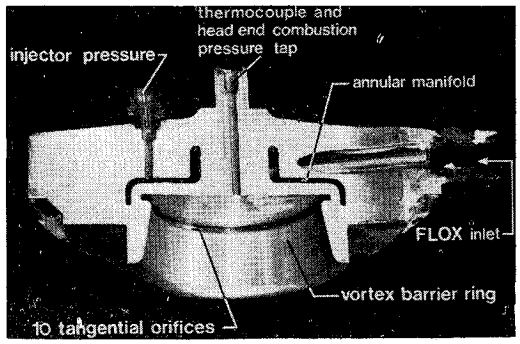

Fig. 3 Vortex-barrier film injector.

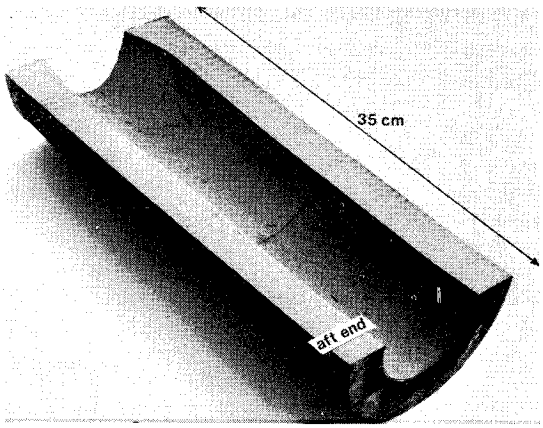

Fig. 4 Post fire grain profile (80 Al/20 PU) for film injector ($t_b = 35$ sec).

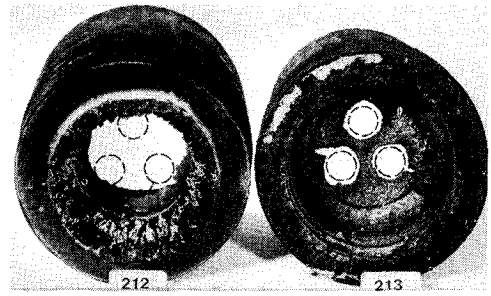

Fig. 5 Three-hole mixing diaphragms after 40-sec test duration with the 60 Al/40 PU/FLOX-40 combination.

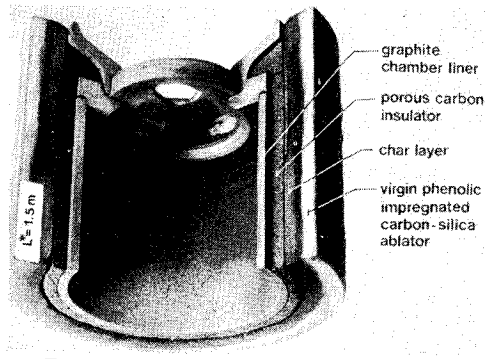

Fig. 6 Ablatively cooled reaction chamber.

rich barrier zone, containing unreacted Al particles. The purpose of the mixing diaphragm is to improve the mixing of oxidizer and fuel flows, thus improving the combustion efficiency.

The experimentally determined erosion rates of the mixing diaphragms were found to differ widely for the two propellant compositions that were investigated. For the 60 Al/40 PU/FLOX-40 system, chemical attack was significant both in the fuel-rich and in the oxidizer-rich periphery, because of reaction of the oxygen with the graphite mixing diaphragm, whereas for the 80 Al/20 CTPB/FLOX-90 system, only the aluminum-carbon reaction in the fuel-rich periphery occurred. In spite of the higher combustion temperature of the 80 Al/20 CTPB/FLOX-90 propellant combination, the lack of oxygen and the fact that fluorine does not react readily with graphite reduces the erosion problem. Satisfactory results in the oxygen-rich periphery were obtained with pyrolitic-carbon-infiltrated graphite, which performed better than any material previously tested, but these mixing diaphragms were eroded almost completely at fuel-rich mixture ratios, as shown by test 212 in Fig. 5.

In order to reduce the chemical attack caused by the aluminum-carbon reaction in the fuel-rich barrier zone, resulting in aluminum carbide (Al_4C_3) formation, tungsten carbide (WC) mixing diaphragms were developed. Unfortunately, the pure WC mixers were very sensitive to thermal shock. A compromise was found in a hot-pressed 80% tungsten carbide/20% graphite composite material, which has the decreased thermal shock sensitivity of pure graphite while minimizing the graphite content and thus reducing Al_4C_3 formation, as is shown by test 213 in Fig. 5.

Solids Deposition Problem

One of the most serious problems was the deposition of solids on the mixing diaphragm and the reaction chamber and nozzle wall, which leads to severe mechanical attack and results in excessive erosion. Chemical analyses indicated that the solid deposits consisted mainly of unreacted aluminum, aluminum nitride (AlN), and aluminum carbide (Al_4C_3), of which the latter is the predominant constituent. It was found that significantly less deposition occurred in tests without a nitrogen purge shut-down sequence, and the corresponding chemical analyses did not indicate any AlN. It therefore was concluded that the motor shut-down sequence was the primary cause of the solid deposition problem. The hot splash-block heated the nitrogen purge gases, which, in turn, melted and reacted with the aluminized fuel grain. The heated, partially reacted aluminum species were stripped away by the shearing forces formed by the purge gas stream and were transported to the glowing graphite mixing diaphragm and the nozzle throat insert, resulting in aggressive destruction of these motor components. In further tests, a nonreactive argon purge was used to eliminate the nitrogen-aluminum reaction, and, additionally, the purge mass flow was increased significantly to improve the cooling effect.

Reaction Chamber

In order to improve the aluminum combustion, a reaction chamber was added, which increases the characteristic length and, therefore, the particle residence time in the motor. A graphite-lined, porous-carbon-insulated, and ablatively cooled reaction chamber, as shown in Fig. 6, was developed to prevent condensation of the aluminum deposits on the chamber wall. The very low thermal conductivity of the ungraphitized porous carbon insulator maintains the high temperature of the graphite chamber liner and minimizes the heat transfer from the combustion zone to the ablative material. In addition, it transpires enough cool pyrolytic gases from the ablative material to cool the graphite liner in order to prevent sublimation.

Nozzle

In order to reduce the nozzle throat erosion rate, a high-density, fine-grade graphite (EK 87) with high thermal conductivity was used for the nozzle throat insert. An asbestos-phenolic molding compound material was used as the nozzle-insert support section. A carbon-phenolic barrier material was applied to the interface between the graphite

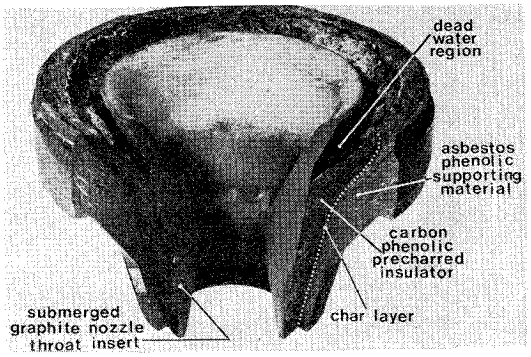

Fig. 7 Submerged nozzle configuration after 60-sec test firing.

nozzle insert and the nozzle support material, since the asbestos-phenolic material was attacked severely by the backside reaction between the melted silica and the glowing graphite nozzle insert.

The carbon-phenolic barrier material was precharred to reduce the thermal conductivity. It serves as an insulator and maintains the nozzle throat surface temperature high enough to prevent condensation of aluminum deposits and conducts heat from the graphite nozzle throat insert sufficient only to prevent sublimation.

In order to protect the nozzle support inlet section from the impinging combustion gas flow, a submerged nozzle entrance design was chosen, as shown in Fig. 7. Because of stagnation of the impinging gas flow at the submerged entry edge and the formation of a local gas recirculation pattern ("dead water region"), significantly less supporting material was eroded than in the case of a conventional nozzle entrance.

Fuel Regression

The average and local fuel regression rates were investigated at total mass fluxes between 2 and 10 g/sec-cm^2. Consequently, the application of the empirical correlations found are restricted to this range of mass fluxes. All test runs were conducted at a chamber pressure of about 10 bar.

The average regression rate $\bar{r}_{\Delta R}$, based upon diameter measurements, was calculated according to

$$\bar{r}_{\Delta R} = \Delta R / t_b \tag{1}$$

whereas the consumed web ΔR was measured at the aft one-third of the grain length (which corresponds to the axial location $0.6\ L_F < x < 0.9\ L_F$). The burning time associated with this distance was defined to be the time between 40% steady-state chamber pressure at ignition to shut-down. Average $\bar{r}_{\Delta R}$ regression rates generally were reproducible within ±3%.

A method of determining the overall average regression rate $\bar{r}_{\Delta m}$ for each test was derived, based on the assumption that the surface of the fuel grain regresses cylindrically throughout the firing, and is defined as

$$\bar{r}_{\Delta m} = \frac{1}{t_b}\left[\left(\frac{\Delta m_F}{\pi \cdot \rho \cdot L_F} + R_0^2\right)^{0.5} - R_0\right] \tag{2}$$

These length-averaged measurements were generally reproducible within ±5%. $\bar{r}_{\Delta m}$ is slightly higher than $\bar{r}_{\Delta R}$, because it includes aft-end grain insulation protrusions and head-end injector disturbances on the fuel port profile.

Local regression rates were obtained by making postfire grain-port diameter measurements at 10 locations along the grain to examine injector effects on the uniformity of the axial and radial regression profiles. Typical results of time-test series are presented in Fig. 8.

Each curve was obtained by means of a separate firing with a new, virgin grain. The average regression rates $\bar{r}_{\Delta R}$ and $\bar{r}_{\Delta m}$ were found to correspond very closely to the local regression

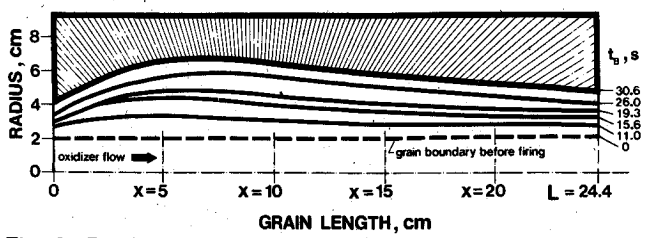

Fig. 8 Postfire grain profiles for hollow-cone spray injector at different burning times.

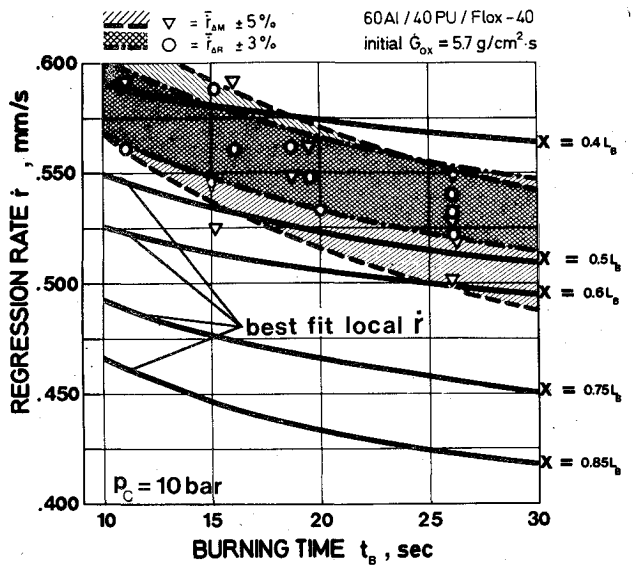

Fig. 9 Comparison of local with average regression rates vs burning time.

rate nearly half-way down the grain, within the interval $0.4\ L_F < x < 0.6 L_F$ (Fig. 9). The average regression rate of the aft one-third of the grain length was correlated with the average oxidizer mass flux. $\dot{G}_{ox}$ is the oxidizer mass flux at the duct cross-sectional area, averaged over the initial and final port areas.

The empirical correlation obtained is

$$\bar{r}_{\Delta R} = a \bar{\dot{G}}_{ox}^{\,0.5} \text{ cm/sec} \tag{3}$$

where $a = 0.034$ for the 60 Al/40 PU/FLOX-40 propellant, and $a = 0.045$ for the 80 Al/20 PU/FLOX-90 propellant composition. The experimental results, shown in Fig. 10, demonstrate that the regression rate of the 80 Al/20 PU/FLOX-90 propellant is about 33% higher than that of the 60 Al/40 PU/FLOX-40 propellant. Higher aluminum loading in the fuel grain, combined with higher fluorine content in the oxidizer, had a significant effect on the regression rate, although it had no particular effect on the mass flux correlation. The slopes of the curves are equal and proportional to the square root of $\dot{G}_{ox}$.

For correlation of the regression rate with the average total mass flux $(\dot{m}_F + \dot{m}_o)/A_p = \bar{\dot{G}}_t$, the local aft-end regression rate $\dot{r}_e$ is used because the most reliable value of total mass flux can be calculated at that point. The empirical regression rate correlation obtained for the 80 Al/20 CTPB/FLOX-90 system is

$$\dot{r}_e = 0.044\ \bar{\dot{G}}_t^{\,0.5} \text{cm/sec} \tag{4}$$

The data are presented in Fig. 11.

The test results obtained are in good agreement with experimental results of other investigators.[2-6] Although the empirical mass flux correlation exponent does not agree with the theoretical value of 0.8 derived in Refs. 7-10, it accounts

for injection and aft-end perturbations not predicted in the theoretical hybrid combustion models.

Performance Characterization

In order to evaluate the combustion efficiency and the motor performance of the highly aluminized propellants, the static test firings were treated as a single impulse in the calculation of average values of c^* and Is efficiencies. Total impulse, chamber pressure-time integrals, and oxidizer flowmeter-time integrals were recorded for this purpose in analog and digital form. From these measured values, the following average parameters were calculated:

Average Mixture Ratio

$$\frac{\overline{O}}{F} = \frac{\Delta m_o}{\Delta m_F} = \frac{\int_0^{t_v} \dot{m}_o \mathrm{d}t}{\Delta m_F} \tag{5}$$

Time-Averaged Characteristic Velocity

$$\overline{c^*} = \frac{\bar{A}_t \cdot \int_0^{t_b} P_c \mathrm{d}t}{\Delta m_F + \int_0^{t_v} \dot{m}_o \mathrm{d}t} \tag{6}$$

Time-Average Specific Impulse

$$\overline{Is}_{\mathrm{exp}} = \frac{I_{\mathrm{tot}}}{\Delta m_p} = \frac{\int_0^{t_b} F \mathrm{d}t}{\Delta m_F + \int_0^{t_v} \dot{m}_o \mathrm{d}t} \tag{7}$$

The average pressure and the average thrust are, respectively,

$$\bar{p}_c = \frac{\int_0^{t_b} p_c \mathrm{d}t}{t_b} \qquad \bar{F} = \frac{\int_0^{t_b} F \mathrm{d}t}{t_b} \tag{8}$$

Theoretical and uncorrected experimental data for c^*_{exp} are plotted in Fig. 12 as functions of oxidizer-fuel mixture ratio.

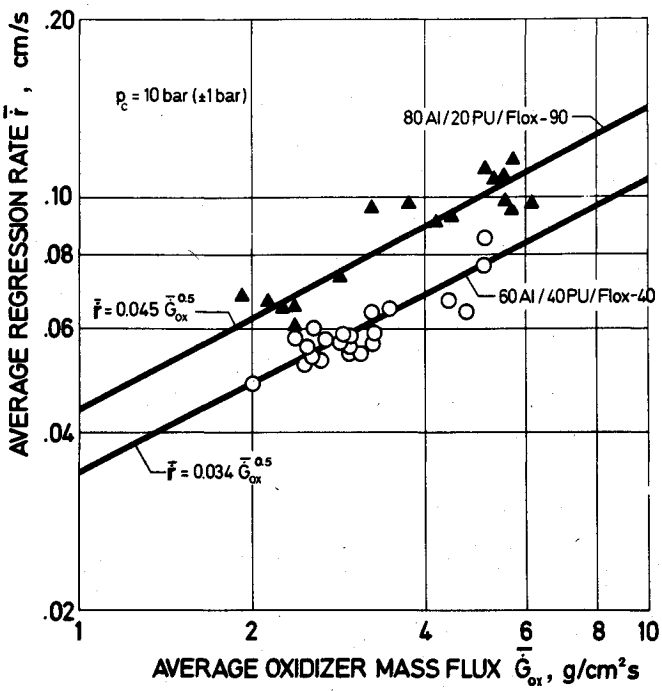

Fig. 10 Comparison of regression rates vs $\bar{G}_{ox}$ for the different propellant combinations.

In the case of the 80 Al/20 PU/FLOX-90 combination, c^*_{exp} could be calculated from measured p_c and A_t within an acceptable standard deviation of less than 5% of the mean value. However, in the case of 60 Al/40 PU/FLOX-40, c^*_{exp} was calculated from the thrust measurements, since the c^* calculations for the small motors used were extremely sensitive to small changes in throat areas.

To correct the delivered specific impulse, the propellant mass flow rate is corrected for inert product discharge and propellant deposition during the test firings. Inert liner and insulation losses due to pyrolysis and erosion of the motor components increase the mass flow rate, whereas the deposits, which were collected and weighed after each firing, reduce the mass flow rate through the nozzle. The combined effects of propellant deposition, inert discharge, and heat rejection were determined in order to correct the measured specific impulse. The total heat loss of the ablatively cooled motor and nozzle is determined in independent motor firings by dropping the entire motor into a water calorimeter within a few seconds after the end of burning, and noting the temperature rise of the water.

This simple method, which includes the heat losses to the entire motor but neglects radiation losses from the nozzle both during and following firing, is capable of giving the order-of-magnitude results required. The heat losses for the ablatively cooled hybrid motor were found to account for 2% of the loss of efficiency. The parameters used to determine the optimum propellant performance for a given motor configuration are the combustion efficiency η_{c^*} and the specific impulse efficiency η_{Is}.

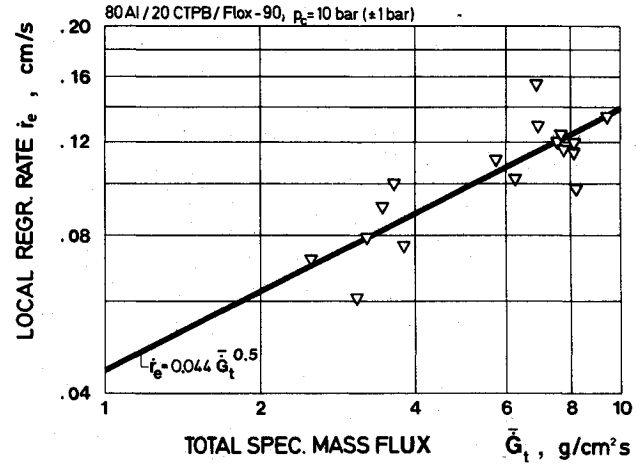

Fig. 11 Aft-end local regression rate vs total mass flux for the 80 Al/20 CTPB/FLOX-90 combination.

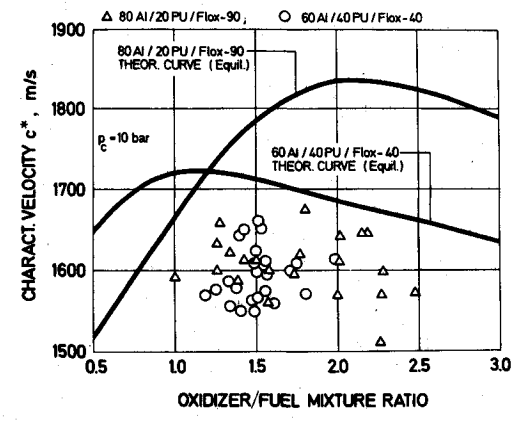

Fig. 12 Delivered, uncorrected c^*_{exp} vs mixture ratio, including values of c^*_{th}.

Effect of Mixing Diaphragm

The importance of geometric parameters to the combustion efficiency for the 60 Al/40 PU/FLOX-40 propellant combination is demonstrated in Table 1. Forced mixing at the aft end of the fuel grain significantly increased the combustion efficiency. Motor firings without a mixing diaphragm result in a much too oxidizer-rich mixture ratio, extreme nozzle erosion, and inherently low combustion efficiency. An effect of mixing diaphragm configuration on the combustion efficiency is observed only between the use of the one-hole and multihole mixing diaphragms; no significant effect is observed between the two-hole, three-hole, or four-hole configurations. In all test firings, the mixing diaphragm is located at the aft end of the fuel grain so that the uniformity of the fuel grain regression is not disturbed.

Effect of Motor Size

The effect of the reaction chamber characteristic length on the combustion efficiency indicates that the main combustion of the aluminum particles occurs in the reaction chamber. Using the optimum mixing diaphragm configuration, the characteristic length was varied between 0.5 and 1.8 m, resulting in $\eta_c{}^*$ and η_{Is} increases (see Table 1).

Effect of Propellant Composition

Table 2 illustrates the results of the corrected combustion and specific impulse efficiencies as a function of different propellant compositions. The low combustion efficiency for the 60 Al/40 PU/LOX (liquid oxygen) combination indicates that the particles leave the motor with only partial combustion. Even at $L^* = 1.5$ m, the particle residence time is too short and the aluminum-oxygen kinetics are too slow to evaporate the unreacted aluminum core through the protective aluminum oxide melt layer in order to obtain complete reaction.

As shown in Table 2, the combustion and specific impulse efficiencies of the 60 Al/40 PU fuels increase with increasing fluorine content in the oxidizer. With FLOX-80, which yields gaseous AlF_3 as the main combustion product, the corrected combustion efficiency approaches 97%, and the corresponding specific impulse efficiency is 95%.

It should be emphasized, however, that the hybrid motors used in these tests are small (150 and 400 N thrust) and that the combustion pressure is only 10 bar (opposed to 70 bar in conventional aluminized composite solid-propellant motors). Consequently, only a very small nozzle expansion ratio ($Ae/At = 2.20$) has been investigated, and the performance increase caused by elimination of the two-phase nozzle flow losses could not be determined.

Combustion Oscillation

No significant difference in $\eta_c{}^*$ and η_{Is} between the 80 Al/20 PU/FLOX-90 and the 80 Al/20 CTPB/FLOX-90 propellant formulations is observed. However, unusually strong pressure fluctuation occurred when using the 80% aluminized polybutadiene-type fuel binder, but this is not considered to be a combustion instability. It appears more to be a kind of "chuffing," as is observed in solid-propellant combustion. The frequency (4-5 cps) is so low that even 80% metal particle loading has no damping effect.

Since under the same conditions no fluctuations with the 80% aluminized polyurethane-type hybrid fuel grains were

Table 1 Effect of mixing diaphragm and reaction chamber L on uncorrected $\eta_c{}^*$ for the 60 Al/40 PU/FLOX-40 combination

mixing diaphragm configuration	reaction chamber L^*, [m]	No. of tests	Ae/At pre-test	Ae/At post-test	$\eta_c{}^*$	std. dev. [± %]
without	1.0	3	2.20	1.34	0.78	6.9
one-hole	1.0	40	2.20	1.96	0.85	1.8
two-hole	1.0	16	2.20	2.00	0.89	2.9
three-hole	1.0	12	2.20	2.13	0.90	3.5
four-hole	1.0	5	2.20	2.13	0.90	5.7
three-hole	0.5	6	2.20	1.68	0.81	4.0
three-hole	1.0	12	2.20	2.13	0.90	3,5
three-hole	1.5	28	2.20	2.15	0.92	1.2
three-hole	1.8	7	2.20	2.18	0.93	4.2

Table 2 Effect of propellant combination on corrected combustion and specific impulse efficiencies (two-hole mixing diaphragm, $L^* = 1.5$ m)

Propellant combination	Primary Product	State	No. of Tests	Standard Deviation c^*_{exp} [±%]	Standard Deviation Is_{exp} [±%]	$\bar{F}$ [N]	$\bar{P}_c$ [bar]	Ac/At pre-test	Ac/At post-test	O/F -	$\eta_c{}^*$ -	$\eta_c{}^*$ corr.	η_{Is} -	η_{Is} corr.
60 Al/40 PU/LOX	Al_2O_3	liq.	22	11.0	9.0	98	7.0	2.20	1.82	1.12	0.81	0.85	0.74	0.77
60 Al/40 PU/FLOX-40	AlOF	gas.	34	5.3	6.7	135	9.4	2.20	2.13	1.34	0.92	0.94	0.90	0.91
60 Al/40 PU/FLOX-80	AlF_3	gas.	17	4.4	4.6	403	10.2	2.20	2.17	2.00	0.96	0.97	0.94	0.95
80 Al/20 PU/FLOX-90	AlF_3	gas.	29	4.6	5.1	347	9.0	2.20	2.26	1.77	0.89	0.92	0.85	0.90
80 Al/20 CTPB/FLOX-90	AlF_3	gas.	19	5.0	6.2	415	12.2	2.20	2.06	1.80	0.88	0.91	0.86	0.90

observed, a possible explanation of the chuffing phenomenon could be that a char layer is formed, which covers the burning grain surface. This layer then would be blown off irregularly by both the oxidizer gas stream and the evolution of pyrolyzation gases from the parent fuel grain. Thus, periodic mass addition and reactions leading to the observed low-frequency pressure oscillations would result. Although the 80 Al/20 PU fuel surfaces were clean after firing, the 80 Al/20 CTPB fuel surfaces were covered with a dark brown char layer.

Conclusions

1) The motor tests indicate that up to 60 to 80 wt% aluminized hybrid solid fuel grains, when combusted with highly fluorinated oxidizers, can perform well and maintain much higher combustion efficiencies than when combusted with oxygen-based oxidizers.

2) An appreciable, further increase in combustion efficiency can be obtained through the choice of the optimum geometry of the motor components, especially that of the mixing diaphragm and reaction chamber.

3) Damage to the nozzle throat insert and mixing diaphragm, which are very critical in obtaining high-accuracy data for proper performance evaluation, is reduced by using advanced composite structural materials.

The experimental results can be summarized as follows:

a) Independent of the propellant composition, the regression rate of the highly aluminized fuel grains varies linearly with the square root of the oxidizer mass flux.

b) Increasing the fluorine content in the oxidizer increases the regression rate and improves the combustion efficiency of the highly aluminized fuels.

c) Increasing the aluminum loading in the solid fuel increases the regression rate but reduces the combustion efficiency.

d) Different types of polymer binders have a noticeable influence on combustion behavior; aluminized PU fuels give smooth steady-state combustion, whereas the aluminized CTPB fuels exhibit a highly fluctuating combustion characteristic.

References

[1] Lips, H.R., "Heterogeneous Combustion of Highly Aluminized Hybrid Fuels," *AIAA Journal*, Vol. 15, June 1977, pp. 777-778.

[2] Lieberherr, J.F., "Les Lois experimentales des Vitesses d'Ablation et leur Application aux Moteurs a Lithergol," ONERA, TP-334, 1966.

[3] Groothoff, C.C., "Ervaringen bij het NLR omtent het hybride verbrandingsprocess," NLR-CC.-58, 1969.

[4] Schmucker, R.H., "Theoretische und experimentelle Beiträge zum Hybridraketenantrieb," *Raumfahrtforschung*, Heft 5, Dec. 1970, pp. 193-202.

[5] Buchheim, R. and Weiler, H., "Untersuchungen an einem Polyäthylen/FLOX-70 Triebwerk," Teil 1, DLR-FB 72-60, 1972.

[6] Weiler, H. and Buchheim, R., "Untersuchungen verschiedener Brennraumgeometrien für ein Polyäthylen/FLOX-70 Triebwerk," Teil 2, DLR-FB 72-61, 1972.

[7] Marxman, G.A., "Combustion in the Turbulent Boundary Layer on a Vaporizing Surface," *10th Symposium (International) on Combustion*, The Combustion Institute, 1965, pp. 1337-1349.

[8] Barrere, M. and Moutet, A., "La Propulsion par Fuses Hybrides," ONERA T.P. 61, 1963.

[9] Smoot, L.D. and Price, C.F., "Regression Rate Mechanisms of Nonmetalized Hybrid Fuel Systems," AIAA Paper 65-56, 1965.

[10] Wooldridge, C.E. and Muzzy, R.J., "Internal Ballistic Considerations in Hybrid Rocket Design," AIAA Paper 66-628, 1966.